Atmosphere-dependent stability and mobility of catalytic Pt single atoms and clusters on γ-Al_2O_3

Caroline Dessal,[a] Alexis Sangnier,[b,c] Céline Chizallet,[*b] Christophe Dujardin,[d] Franck Morfin,[a] Jean-Luc Rousset,[a] Mimoun Aouine,[a] Matthieu Bugnet,[e] Pavel Afanasiev,[a] Laurent Piccolo[*a]

[a.] Univ Lyon, Université Claude Bernard - Lyon 1, CNRS, IRCELYON - UMR 5256, 2 Avenue Albert Einstein, F-69626 VILLEURBANNE CEDEX, France. *E-mail: Laurent.Piccolo@ircelyon.univ-lyon1.fr
[b.] IFP Energies nouvelles, Rond-point de l'échangeur de Solaize, 69360 Solaize, France. *E-mail: Celine.Chizallet@ifpen.fr
[c.] IFP Energies nouvelles, 1 et 4 avenue de Bois-Préau, 92852 Rueil-Malmaison, France.
[d.] Univ. Lille, ENSCL, UMR 8181, Unité de Catalyse et Chimie du Solide, Cité Scientifique Bât. C3, 59655 Villeneuve d'Ascq Cedex, France.
[e.] Univ Lyon, INSA Lyon, UCBL Lyon 1, MATEIS, UMR 5510 CNRS, 7 Avenue Jean Capelle, F-69621 Villeurbanne Cedex, France.

Atomically dispersed metals promise the ultimate catalytic efficiency, but their stabilization onto suitable supports remains challenging owing to their aggregation tendency. Focusing on the industrially-relevant Pt/γ-Al_2O_3 catalyst, *in situ* X-ray absorption spectroscopy and environmental scanning transmission electron microscopy allow us to monitor the stabilization of Pt single atoms under O_2 atmosphere, as well as their aggregation into mobile reduced subnanometric clusters under H_2. Density functional theory calculations reveal that oxygen from the gas phase directly contributes to metal-support adhesion, maximal for single Pt atoms, whereas hydrogen only adsorbs on Pt, and thereby leads to Pt clustering. Finally, Pt cluster mobility is shown to be activated at low temperature and high H_2 pressure. Our results highlight the crucial importance of the reactive atmosphere on the stability of single-atom *versus* cluster catalysts.

1. Introduction

Single-atom catalysts (SACs) have recently emerged as a promising new class of atom-efficient materials for a variety of reactions usually catalysed by supported metal nanoparticles, with possible applications in e.g. chemical synthesis and energy production.[1–4] While many demonstrations of successful SAC preparation and evaluation have been published to date,[5–15] little is known about the stability and dynamics of isolated atoms and other subnanometric metal species under reaction conditions.[16–18] Controlling such parameters is crucial before considering any practical application of SACs at the industrial level. Pt/γ-Al_2O_3 is a prototypical system in heterogeneous catalysis, used for numerous applications such as car exhaust pollution abatement, petrochemistry, and oil refining.[19–23] In 1996, the presence of Pt dimers and trimers on γ-Al_2O_3 was demonstrated using scanning transmission electron microscopy (STEM).[24] More recently, it was shown that Pt can be atomically dispersed on alumina by conventional impregnation-calcination methods through anchoring on coordinately unsaturated Al^{3+} sites.[25,26] Such Pt/γ-Al_2O_3 SACs were found active for CO oxidation.[8] However, single Pt atoms appear unstable against H_2 exposure, forming flat subnanometric clusters of one to two atomic layers.[27,28] Similar alumina-supported Pt "rafts"[27,29], obtained upon impregnation-calcination-reduction of Pt precursors,[28,30–36] constitute the active phase in catalytic reforming of naphtha to gasoline, which is among the most important catalytic processes in refineries.[30,37] The size, morphology and electronic properties of these subnanometric clusters strongly depend on their chemical environment.[29,38–42] In particular, pre-exposure to O_2 was shown to limit the H_2-induced sintering of Pt nanoparticles supported on alumina.[43] However, a clear and general description of the preferred Pt nuclearity (number of metal atoms) and structure at the various stages of the catalyst synthesis and exposure to reactive atmospheres, taking into account the reactant adsorption and coverage, was lacking. Herein, we provide an atomic-scale view of the nucleation process of Pt single atoms (SAs) and their stability or clustering. *In situ* X-ray absorption spectroscopy (XAS) shows the formation of single Pt atoms over alumina under oxidative treatment, and their destabilization into subnanometric clusters under reductive treatment. Environmental STEM (E-STEM) experiments under H_2 or O_2 reveal the gas- and temperature-dependent mobility of the Pt entities. Finally, Density Functional Theory (DFT) calculations allow us to rationalize these behaviours in terms of nuclearity and O/H coverage, which govern the cluster size, shape and interaction with the support.

2. Methods

2.1. Catalyst preparation

Tetraamineplatinum(II) nitrate (Alfa Aesar, >50 wt% Pt) and platinum(II) acetylacetonate (Alfa Aesar, >48 wt% Pt) were used as Pt precursors without further purification. The γ-Al_2O_3 powder (Sasol Puralox SCFa-140, >97.0 % Al_2O_3) was calcined in air at 600 °C for 3 h before use. For catalyst preparation, 2.0 g of alumina powder was impregnated with 2 mL of an aqueous solution of $Pt(NH_3)_4(NO_3)_2$ (incipient wetness impregnation, 0.3Pt-imp sample) or added to a 25 mL ethanol solution of $Pt(acac)_2$ (wet impregnation, 0.5Pt-imp sample), and stirred at ambient temperature for 5 h. For 0.3Pt-imp, the solid was dried in air at 60 °C overnight. For 0.5Pt-imp, ethanol was evaporated with a vacuum rotary evaporator at 80 °C and the solid was dried under vacuum at 80 °C overnight. The resulting powders were calcined in air (30-50 mL/min) at 300 °C for 2 h (2 °C/min ramp). The Pt loadings

of the 0.3Pt and 0.5Pt samples were find equal to 0.30 and 0.51 wt%, respectively, by inductively coupled plasma - optical emission spectroscopy (ICP-OES, Horiba Jobin Yvon). It was observed that, for a given Pt loading, incipient wetness impregnation and wet impregnation lead to similar Pt dispersion and CO oxidation performance, the final calcination being the key parameter.[44]

2.2. Scanning transmission electron microscopy

The STEM experiments were performed with a FEI Titan ETEM G2 electron microscope operated at 300 keV equipped with a Cs image aberration corrector. The extraction voltage, camera length, acceptance angles, STEM resolution and probe current are 4500 V, 245 mm, 29.2-146 °, 0.14 nm and <0.1 nA, respectively. For sample preparation, the powder was crushed and dispersed in ethanol with ultrasonication, dropped onto a TEM grid or chip, and dried by a lamp. To avoid contamination during analysis and remove all residual carbon, the samples were Ar plasma-cleaned for 20 s (Plasma Prep 5, GaLa Instrumente). A simple-tilt FEI sample holder and holey carbon-coated 200 mesh Cu grids were used for high-vacuum analyses at RT. A DENS Solutions sample holder and SiN_x S5 chips (20 nm thickness, 1300 °C max.) were used for the environmental experiments. The movies (S1 and S2) were obtained from alignment of image series. No filtering was applied on the STEM images.

2.3. X-ray absorption spectroscopy

The local structure of Pt species was investigated by XAS in transmission mode on the ROCK beamline at the SOLEIL synchrotron. X-ray absorption spectra at the L3 edge of Pt were recorded. The powder samples were placed inside a plug-flow *operando* cell composed of a sample holder fitted into a heated block. The cell was connected to a gas distribution system allowing for careful control of the gas flows at atmospheric pressure.[45] *In situ* thermal treatments were applied from RT to 300 °C under air flow (10^5 Pa, 50 mL/min, 4 °C/min) or H_2 flow (10^5 Pa, 30 mL/min, 5 °C/min). The reactor was flushed for 10 minutes under He between the oxidative and the reductive treatments. Data merging and preliminary analysis were carried out using ATHENA software,[46] EXAFS fitting was performed using VIPER program.[47] Wavelet analysis was done using wavelet.m MATLAB applet.[48]

2.4. DFT calculations

Periodic DFT calculations were performed with the VASP code[49,50] with the PBE (Perdew, Burke, and Ernzerhof) exchange-correlation functional.[51] The projected augmented wave (PAW) method [52] was used to describe the core-electrons interactions and the plane wave basis set was limited to a kinetic cut-off energy of 400 eV. The convergence criterion for the electronic self-consistent field relaxation was fixed to 10^{-6} eV, and all calculations were performed at the Γ-point.

The starting points of the calculations are the $Pt_{1\text{-}13}/\gamma\text{-}Al_2O_3(100)$ cluster models established in refs.[53,54]. In these models, Pt_1, Pt_2 and Pt_{13} are stabilized by Pt-O and Pt-Al bonds on the (100) surface, which exhibits pentacoordinated Al atoms, and two- and three-fold coordinated O atoms.[55] The role of Al_V in the stabilization of Pt, in particular single atoms, has been emphasized by Kwak and coworkers.[25,26] H_2 and O_2 adsorptions on the Pt_{13} clusters were simulated in refs. [54] and [56], respectively. In the present work, we calculated H_2 and O_2 adsorption on Pt_1 and Pt_2 clusters by geometry optimizations (convergence criterion: all forces lower than 0.02 eV/Å, relaxed atoms: two of the four alumina layers, and the whole cluster with adsorbates). The chemical potential of a given single atom or cluster for a given O_2/H_2 pressure was calculated from the O_2/H_2 adsorption free energy, taking into account the vibrational degrees of freedom of the supported Pt entities and the alumina surface, in a similar manner as explained in, e.g., ref.[57] The latter were estimated from harmonic frequency calculations, with a displacement of ±0.01 Å in each direction for all relaxed atoms. The Hessian matrix was then calculated by the finite difference method. The nature of the most stable system at a given temperature and O_2/H_2 partial pressure is given by the lowest (most negative) adsorption free energy.

We quantified the sintering Gibbs free energies of Pt_1X_m/Al_2O_3 (X=H or O) into Pt_2X_n/Al_2O_3, and of Pt_2X_n/Al_2O_3 into $Pt_{13}X_p/Al_2O_3$. m, n and p are the numbers of H or O atoms adsorbed on the clusters in their most stable state for given temperature and X_2 pressure conditions. The reactions taking place during sintering are given in equations 1 (Pt single atom to Pt_2 dimer) and 2 (Pt dimer to Pt_{13} cluster). The brackets depict the cell involved in the calculation. For example, $\{Al_2O_3\}$ is a unit cell containing only the alumina surface.

$$2\{Pt_1X_m/Al_2O_3\} = \{Pt_2X_n/Al_2O_3\} + \{Al_2O_3\} + \frac{2m-n}{2}X_{2(g)} \quad (1)$$

$$\frac{13}{2}\{Pt_2X_n/Al_2O_3\} = \{Pt_{13}X_p/Al_2O_3\} + \frac{11}{2}\{Al_2O_3\} + \frac{\frac{13n}{2}-p}{2}X_{2(g)} \quad (2)$$

$\Delta_r G_{sint(1)}$ and $\Delta_r G_{sint(2)}$ are the corresponding sintering Gibbs free energies expressed per platinum atom, given by equations 3 and 4. A negative value means that sintering is favoured, whereas a positive value means that the Pt_1 SAC (for $\Delta_r G_{sint(1)}$) or the Pt_2 form of the system (for $\Delta_r G_{sint(2)}$) is thermodynamically more stable.

$$\Delta_r G_{sint(1)} = \frac{1}{2} \times \left(\frac{2m-n}{2} G_{(X_{2(g)})} + G_{\{Al_2O_3\}} + G_{\{Pt_2X_n/Al_2O_3\}} - 2G_{\{Pt_1X_m/Al_2O_3\}}\right) \quad (3)$$

$$\Delta_r G_{sint(2)} = \frac{1}{13}\left(\frac{\frac{13n}{2}-p}{2} G_{(X_{2(g)})} + \frac{11}{2} G_{\{Al_2O_3\}} + G_{\{Pt_{13}X_p/Al_2O_3\}} - \frac{13}{2} G_{\{Pt_2X_n/Al_2O_3\}}\right) \quad (4)$$

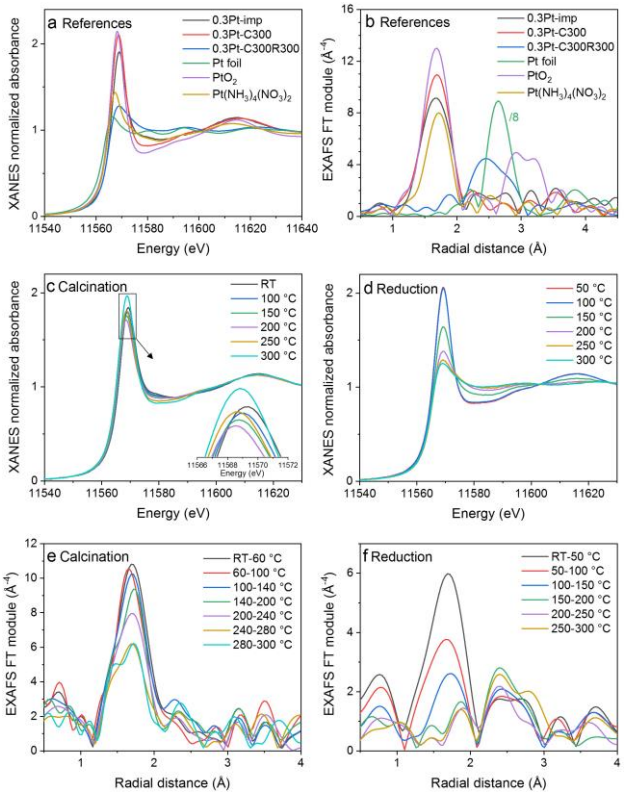

Fig. 1 XANES spectra (a) and EXAFS Fourier transform modules (b) of 0.3 wt% Pt/γ-Al_2O_3 sample, either fresh (0.3Pt-imp), or after calcination in air flow at 300 °C (0.3Pt-C300), or after subsequent reduction in H_2 flow at 300 °C (0.3Pt-C300R300), *vs.* standards. Evolution of XANES spectra (c,d) and EXAFS FT modules (e,f) for the 0.3Pt-imp sample during calcination in air flow (c,e) and subsequent reduction in H_2 flow (d,f) from RT to 300 °C.

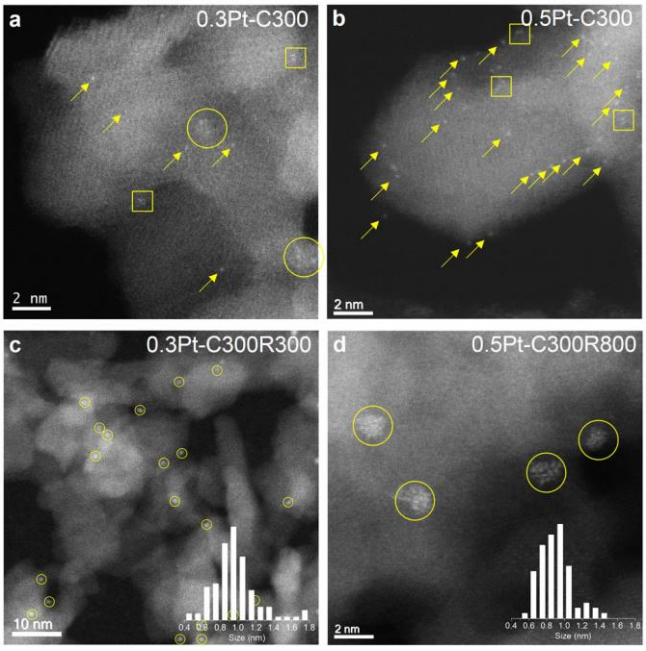

Fig. 2 Representative STEM-ADF images of the Pt/γ-Al_2O_3 catalysts: a) As-prepared 0.3Pt-C300 sample. b) As-prepared 0.5Pt-C300 sample. c) 0.3Pt-C300 sample after H_2 treatment during XAS experiment (C300R300). d) 0.5Pt-C300 sample after H_2 treatment during E-STEM experiment (C300R800). Arrows, squares and circles indicate single Pt atoms, multimers and clusters, respectively. Inserts of c) and d) show Pt particle size histograms.

3. Results

3.1. Formation of single Pt atoms and their stability under oxidizing atmosphere

The X-ray absorption near-edge structure (XANES, Fig. 1a) and extended X-ray absorption fine structure (EXAFS, Fig. 1b) contributions of an impregnated $Pt(NH_3)_4(NO_3)_2$/γ-Al_2O_3 (0.3 wt% Pt) sample (further designated as 0.3Pt-imp), and of the same

solid calcined in air (0.3Pt-C300) were compared to references. The evolution of XANES spectra during heating in air (Fig. 1c) was analysed *in situ* as a function of the temperature. The tetraammine Pt(II) nitrate precursor is partially oxidized to Pt(IV) when impregnated on alumina, as the intensity of the XANES white line is significantly increased and the spectrum becomes similar to that of the PtO_2 reference (Fig. 1a). From EXAFS (Fig. 1b), the first-shell coordination number (CN) of platinum in the 0.3Pt-imp sample (CN = 5.2 ± 0.6, Table S1) is higher than that of the pure precursor (CN = 4). However, neither conventional EXAFS fitting (Fig. S1) nor wavelet analysis (Fig. S2) allowed us to detect a heavy (Pt) neighbour in the second coordination shell, which is present in the PtO_2 reference. This observation is compatible with previous EXAFS measurements on Pt catalysts supported on various materials.[8,33,58–60] Therefore, in the impregnate, we suspect that Pt on the surface of alumina is present as SAs in a local oxygen environment, similar to that of Pt(IV) in PtO_2. During the subsequent temperature-programmed heating in air from RT to 300 °C, the decrease of the white line intensity and the shift of the main jump to lower energies indicate partial reduction of Pt(IV) species between 100 °C and 200 °C, followed by re-oxidation above 200 °C (Fig. 1c). The Pt(IV)-like oxidation degree suggested by XAS for the $Pt(NH_3)_4(NO_3)_2/Al_2O_3$ impregnate –instead of Pt(II) for the molecular precursor– can be due to the presence of neighboring physisorbed O_2 molecules around Pt at room temperature. These molecules are prone to desorption upon thermal heating, until they may also dissociatively chemisorb on Pt at higher temperature, which could explain the observed decrease then increase of the oxidation degree. Moreover, the initial thermal decomposition of the Pt precursor impregnated on alumina may also transiently and partially reduce Pt at low temperature.

After cooling back down to RT in air (0.3PtC300, Fig. 1a), a PtO_2-like environment is obtained, with a Pt-O coordination number of 5.5 ± 0.8 and a Pt-O radial distance of 2.03 ± 0.03 Å (versus 6 and 2.04 ± 0.02 for PtO_2, see Table S1).

For STEM investigations, a higher Pt loading (0.5 wt%, 0.5Pt sample) was also chosen in order to simultaneously visualize a significant number of particles. STEM images in annular dark field (ADF) detection mode of 0.3Pt-C300 (Figs. 2a and S3) and 0.5Pt-C300 (Figs. 2b and S4) samples confirm the presence of SAs (characteristic white spot size of 0.15 ± 0.02 nm,[61] Fig. S5) on calcination treatment. A small fraction of multimers (few-atom clusters) and 1 nm clusters can also be observed. E-STEM experiments confirm the stability of SAs also under low-pressure oxygen atmosphere (see Section 3.3).

Our results showing the stabilizing effect of oxidizing conditions on Pt dispersion are consistent with other works on several metal/oxide systems, in line with the facts that SAC preparation often ends with an air calcination and that oxidative thermal treatment is a common catalyst regeneration process.[1,17,25,43,62] Density functional theory (DFT) calculations were undertaken to provide an atomistic justification of the SAC stability in calcination conditions (300 °C, 0.2 10^5 Pa O_2), and describe the Pt environment for supported Pt_1O_x (SA), Pt_2O_x (dimer) and $Pt_{13}O_x$ (cluster). Figs. 3a-b (for Pt_1 and Pt_2) and S13 report the thermal stability of each supported Pt_yO_x entity. Fig. 4a-c depicts the most stable systems (Pt_1O_4, Pt_2O_4, $Pt_{13}O_{22}$) together with the values of the Gibbs free energy for sintering from Pt_1 to Pt_2 then Pt_{13}. The affinity of Pt for oxygen is stronger (higher O/Pt ratio) at small cluster sizes, in agreement with previous findings for non-supported clusters.[63] We also expect from the calculation oxygen desorption in air at 270°C, which is similar to a surface reduction. The calculation of the sintering (clustering) free energy shows that Pt_1, decorated by 4 O atoms, remains in the form of SAs in these conditions, without forming Pt_2O_x or $Pt_{13}O_y$ clusters (positive sintering free energies). Notably, the sintering free energies calculated in the absence of adsorbate at the same temperature of 300 °C (Fig. 3g-i) suggest a possible sintering from Pt_1 to Pt_{13}, even if a slightly positive sintering free energy is calculated from Pt_1 to Pt_2. Thus, taking into account the O coverage and its evolution as a function of the nuclearity is crucial, otherwise reverse conclusions can be reached.[26] This leads us to invoke interaction modes different from the one proposed when focusing on the PtO_2 stoichiometry only.[64]

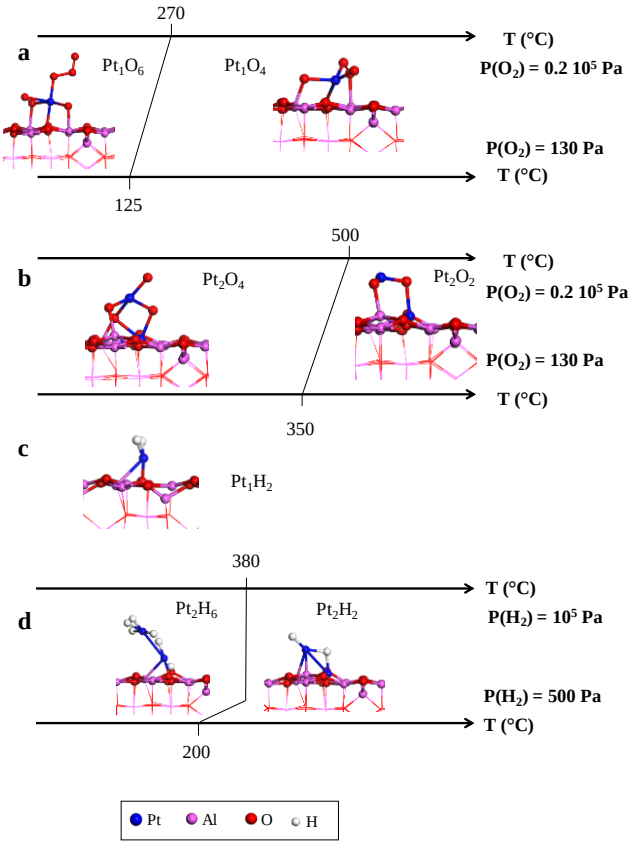

Fig. 3 Structures of the most stable oxidized (a,b) and reduced (c,d) Pt_1 and $Pt_2/\gamma\text{-}Al_2O_3(100)$ clusters in XAS (upper axis) and E-STEM (lower axis) conditions. Pt_1H_2 (c) is the stable species in all reducing conditions for Pt_1.

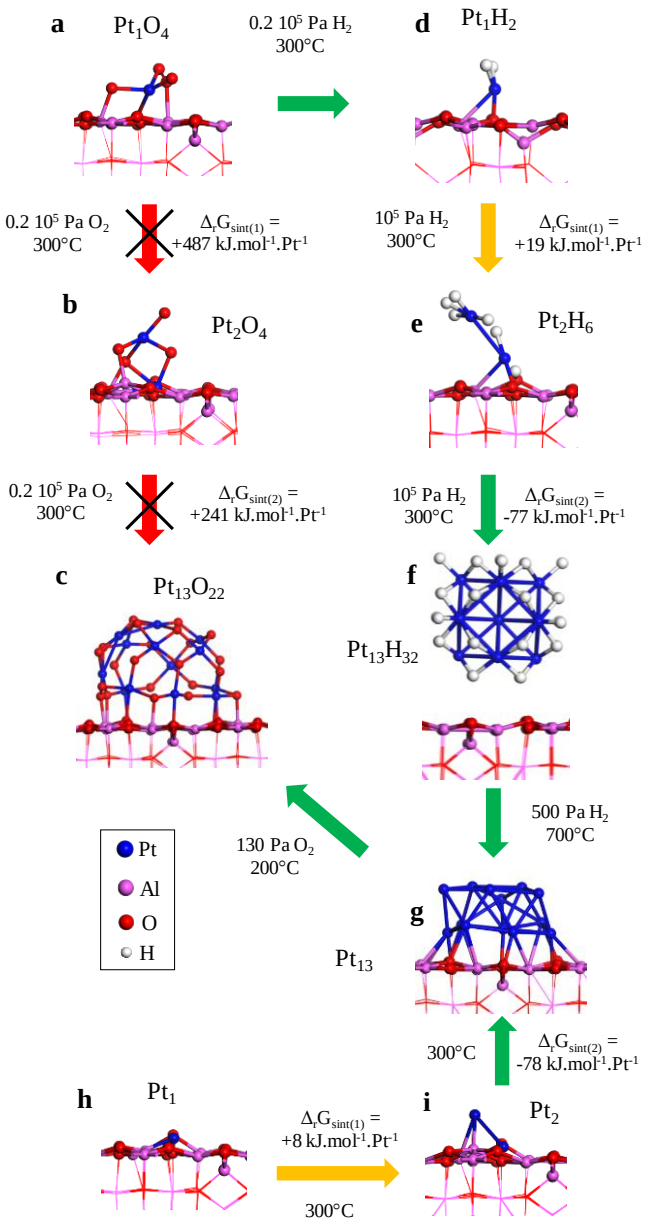

Fig. 4 Most stable systems found by DFT calculations for each nuclearity (Pt_1, Pt_2, and Pt_{13} supported on γ-Al_2O_3(100)) depending on experimental conditions. The sign of the sintering free energy indicates whether clustering is possible or not from a thermodynamic point of view. a) Pt_1O_4, most stable in calcination conditions (10^5 Pa air, 0.2 10^5 Pa O_2, 300 °C). b) Pt_2O_4. c) $Pt_{13}O_{22}$.[56] d) Pt_1H_2, obtained under reduction conditions (10^5 Pa H_2, 300 °C). e) Pt_2H_6. f) $Pt_{13}H_{32}$,[65] obtained from Pt_2H_6 in reduction conditions. g) $Pt_{13}H_0$,[53] obtained in typical E-STEM conditions (500 Pa H_2, 700 °C), h) Pt_1 free from adsorbate[54] and i) Pt_2 free from adsorbate,[54] both modelled as reference systems.

The negative free energy (-58 $kJ.mol^{-1}.at_{Pt}^{-1}$) for sintering of supported $Pt_{13}O_{22}$ into bulk PtO_2 (Fig. S13 and Supplementary Theoretical Methods S1) shows that this trend can be limited depending on the concentration of SA. In the PtO_4 model, the Pt atom is connected to 4 O atoms, the shortest bond (1.76 Å) corresponding to a terminal O atom (not bonded to the support). Pt_1 is strongly anchored onto the support through 3 Pt-O bonds (1.91, 1.95 and 2.11 Å) and 4 O-Al bonds. The average of the 4 Pt-O bond lengths is 1.93 ± 0.14 Å. In the most oxygenated system, Pt_1O_6, the platinum atom is surrounded by 5 O atoms, with an average bond length of 1.98 ± 0.11 Å. These values are in reasonable agreement with the EXAFS data for the coordination number (5.5 ± 0.8) and the radial distance (2.03 ± 0.03 Å) in the calcined catalyst. In the Pt_2O_4 model, 8 Pt-O bonds exist, but only 4 O atoms participate in metal-support bonds, due to the upward position of one of the Pt atoms. The amount of adsorbed oxygen is thus directly linked to the ability to form Al-O bonds between dissociated O_2 and the support at the platinum/support interface.
From Pt_1O_4 to Pt_2O_4 and then $Pt_{13}O_{22}$, the O/Pt ratio decreases (4, then 2, then 1.69), meaning that sintering is accompanied by O_2 desorption, which is favoured from an entropic point of view. Thus, the stabilization of the single atoms with respect to Pt_2 and Pt_{13} species cannot be of entropic nature, and is thus of enthalpic nature. The latter can be explained by the higher O/Pt ratio for Pt_1, corresponding to a higher gain in enthalpy due to the larger number of dissociated O_2 molecules per platinum atom, thus with more numerous Pt-O and Al-O-Pt bonds. This explains the optimal stabilization of single Pt atoms.

3.2. Response to H_2

In situ XAS was also performed to analyse the response of the Pt/γ-Al_2O_3 SACs to H_2 atmosphere. Heating from RT to 300 °C under H_2 flow following the previous *in situ* formation of the 0.3Pt-C300 SAC through air calcination, shows a progressive and strong decrease of the XANES white line intensity (Fig. 1d), corresponding to the formation of Pt(0) species.[66] The presence of isobestic points attests that the initial oxidized state transforms directly to reduced Pt without involvement of any stable intermediate state. *In situ* EXAFS observations reveal an increase of the Pt-Pt/Pt-O FT component ratio already below 50 °C (Fig. 1f), which is further supported by clear Pt-Pt neighbour contributions after cooling back the sample to RT (Figs. 1b, S1 and S2). However, no large metallic Pt particles are formed, but Pt clusters with Pt-Pt CN lower than 5 (Table S1). At the same time, a light neighbour (O), belonging probably to the oxide support, is detected.

STEM analyses performed after the XAS experiments confirm the partial clustering of Pt SAs under H_2, and its increased probability at higher temperature (Figs. S8 and 2c/S9 correspond to treatments at RT and up to 300 °C, respectively).

The dynamics of Pt clusters under H_2 was then investigated by E-STEM from RT up to 800 °C. Figure 5 reveals their significant mobility at temperatures lower than *ca*. 200 °C. The clusters are overall stable in size (0.88 ± 0.07 nm), with strikingly similar size distributions before (average size 0.85 nm) and after (0.90 nm) the heating period under H_2 (Fig. S6a, see also STEM images of Figs. 2d and S7). Only a slight gradual increase in size above *ca*. 400 °C can be distinguished (Fig. S6b). Noticeably, the same average value of 0.88 nm was measured for 0.35 wt% Pt supported on chlorinated γ-Al_2O_3 after high-temperature treatment in H_2.[28]

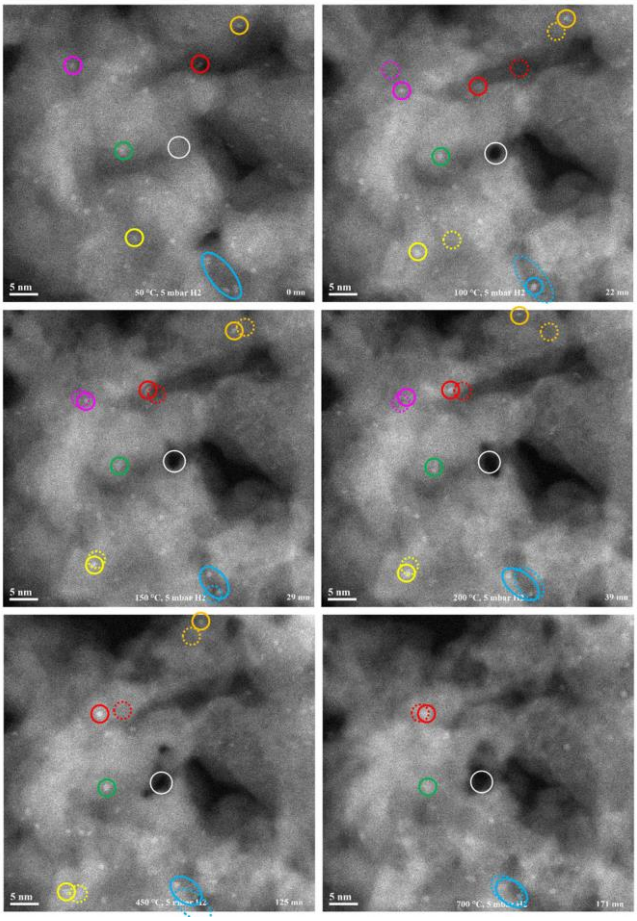

Fig. 5 STEM-ADF images recorded at increasing times (0, 22, 29, 39, 125 and 171 min) and temperatures (50, 100, 150, 200, 450 and 700 °C) for the 0.5 wt% Pt/γ-Al_2O_3 catalyst (0.5Pt-C300 sample) under 500 Pa H_2. Coloured circles show individual clusters while the blue oval shows a group of clusters. The central white circle shows the location used for beam focus tuning. From one frame to the next, an identical location is indicated as a dotted circle with the same colour. The full movie (S1) can be found in ESI.

To rationalize and quantify the H_2-induced clustering and mobility effects, the interaction of hydrogen with supported Pt_1, Pt_2 and Pt_{13} clusters was modelled through DFT calculations. Stability domains were calculated as a function of the temperature and the H_2 partial pressure (Figs. 3c-d and S14). In the absence of adsorbate, the Pt_{13} cluster is expected to be of biplanar morphology,

interacting through Pt-Al and Pt-O bonds with the support.[53] Note that the largest dimension of the biplanar Pt_{13} cluster (Fig. 3g) is 0.9 nm, consistently with the experiments. In the presence of H_2 at high pressures and/or at low temperatures, the cluster was found to reconstruct in a cuboctahedron and disconnect from the support.[42,65] This is connected to the proposal, from EXAFS observations, of "interfacial hydrogen" between the cluster and the support.[29,59,67] Fig. 4d-f summarizes the most stable species (Pt_1H_2, Pt_2H_6, $Pt_{13}H_{32}$) identified in reduction conditions (10^5 Pa H_2, 300 °C). Hydrogen spillover was found marginal in these conditions, in agreement with the non-reducible nature of the support.[68] The calculation of the sintering free energy shows that, under H_2, sintering is a favourable process from a thermodynamic point of view, contrary to what is observed in calcination conditions. Hydrogen adsorbed on platinum behaves very differently from oxygen. Its interaction with the support is much weaker, in particular for the Pt_1H_2 system where the two H atoms adsorb in an upward geminal mode on Pt (Figs. 3d and S14a). On the contrary, for the Pt_1O_4 system, the O atoms are also strongly bonded to the support *via* Al-O bonds. By increasing the nuclearity to Pt_2, the second Pt atom, disconnected from the support, interacts with many more H atoms (4), yielding a hydrogen-richer system (Pt_2H_6). This trend is confirmed for Pt_{13} ($Pt_{13}H_{32}$), which is thus more stable from an enthalpic point of view.

From Pt_1 to Pt_{13}, the H/Pt ratio increases from 2 to 2.5. The sintering however occurs (negative sintering free energy $\Delta_rG_{sint(1)} + \Delta_rG_{sint(2)}$, Fig. 4) despite the need for adsorbing extra H_2 molecules from the gas phase, with a high loss in entropy. Thus, here again, the ability of platinum to sinter under H_2 atmosphere is driven by enthalpic aspects, in spite of opposite entropic contributions.

The conclusion is reversed with respect to the behaviour under O_2, due to the higher affinity of hydrogen for platinum rather than for the support, whereas oxygen is better stabilized at the platinum/support interface rather than on Pt alone. SAs are the preferred systems to increase the amount of O atoms (per Pt atom) at the interface between the metal and the support, whereas clusters are the optimal systems to increase the number of H-Pt bonds while minimizing the cluster/support interaction. The sintering free energy from supported $Pt_{13}H_{32}$ to bulk platinum (Supplementary Theoretical Methods S1) is estimated at -145 kJ mol^{-1} at_{Pt}^{-1}, which means that sintering could go far beyond 1 nm particles in the presence of H_2. However, from STEM experiments, the particle size hardly exceeds 1 nm. One may think of a kinetic limitation for sintering. Charge analysis[42,65] shows that for the $Pt_{13}H_{32}$ model, the Pt clusters are cationic with negatively charged H atoms. This charged shell is likely to prevent cluster coalescence by mutual electrostatic repulsion. Above *ca*. 200 °C up to 800 °C, the clusters almost immobilize (on an overall time period of 2 h), as shown by the E-STEM image series of Fig. 5. Consistently, from DFT calculations, cluster mobility is expected below 200 °C under 500 Pa H_2, simultaneously to the biplanar-to-cuboctahedron transition. Under 10^5 Pa H_2 (XAS conditions), the loss of metal-support interaction for the clusters is expected below 330 °C (Fig. S14).

3.3. Response of Pt clusters to O_2

In order to evaluate the possible mobility / redispersion of Pt species under O_2, Pt clusters and SAs were monitored by E-STEM under 130 Pa O_2 (Figs. S10-S12, Movie S2). Both types are quasi-immobile under O_2 between RT and 800 °C. DFT calculations show that the Pt_{13} clusters are strongly oxidized (from 1.5 to 1.8 O per Pt atom) in these conditions, and remain strongly bonded to the support (Figs. 4c and S13c) through mainly Pt-O and O-Al bonds. The metal-support interaction energy (Fig. S13) for Pt_{13} clusters substantiates the enhancement of the cluster mobility under H_2, *versus* the enhanced stacking to the support under O_2, in agreement with the experiments. From a thermodynamic point of view, redispersion of the clusters should be feasible as reverse sintering reactions (Fig. 4a-c), and has been observed for Pt/ Al_2O_3 catalysts between 300 °C and 600 °C under atmospheric-pressure oxygen.[69] However, kinetic limitations likely have to be overcome, which would explain why redispersion is not observed under the present experimental conditions.

The mechanisms of O_2-induced stabilization and H_2-induced destabilization revealed here for Pt/Al_2O_3 SACs may qualitatively apply to other metal/oxide systems, as related behaviors have been recently observed, without theoretical rationalization of the underlying mechanisms, for e.g. Pt/CeO_2 [12,17], Pt/Fe_2O_3 [70], Pt/MCM-22 [18], and Ir/FeO_x [71].

4. Conclusions

By a combination of *in situ* XAS at atmospheric pressure, STEM after *ex situ* thermal treatments, E-STEM at low pressure, and DFT calculations taking into account realistic temperature and pressure, the present work unravels the mechanisms and conditions in which SACs remain stable or sinter, in the case of the prototypical $Pt/\gamma\text{-}Al_2O_3$ system. It is shown for the first time that oxygen atoms originating from gas-phase O_2 serve as ligands that stabilize the Pt SAC, in addition to the alumina support. Indeed, in O_2-rich atmosphere, owing to the strong Pt-O-Al bonding, Pt SAs are stable, immobile and strongly oxidized. In contrast, under H_2, SAs aggregate into subnanometric clusters, which are mobile above a critical H coverage owing to the strong Pt-H interaction at the expense of the metal-support adhesion. As-prepared SACs may thus not keep their single-atom nature in all catalytic applications, in particular when H_2 is present in the atmosphere.

Conflicts of interest

There are no conflicts to declare.

Acknowledgements

L. Roiban and T. Epicier (MATEIS) are acknowledged for help in TEM experiments. S. Belin (SOLEIL), C. Zlotea and A. Malouche (ICMPE) are acknowledged for support with XAS experiments at the ROCK beamline of SOLEIL synchrotron. N. Cristin and P. Mascunan (IRCELYON) are acknowledged for ICP analyses. P. Raybaud, A. Nicolle and M. Matrat (IFP Energies nouvelles) are acknowledged for discussions about the DFT calculations. French government (C. Dessal's PhD funding), Région Auvergne-Rhône Alpes (CMIRA project) and LABEX iMUST ANR-10-LABX-0064/ ANR-11-IDEX-0007 (C. Dessal's PhD support) are acknowledged for financial support. The XAS work was supported by a public grant overseen by the French National Research Agency (ANR) as part of the "Investissements d'Avenir" program (ANR-10-EQPX-45). The STEM work was performed at the Lyon-St-Etienne consortium for electron microscopy.

References

1 J. Liu, *ACS Catal.*, 2017, **7**, 34–59.
2 H. Yan, C. Su, J. He and W. Chen, *J. Mater. Chem. A*, 2018, **6**, 8793–8814.
3 J. Su, R. Ge, Y. Dong, F. Hao and L. Chen, *J. Mater. Chem. A*, 2018, **6**, 14025–14042.
4 A. Wang, J. Li and T. Zhang, *Nat. Rev. Chem.*, 2018, **2**, 65–81.
5 S. F. J. Hackett, R. M. Brydson, M. H. Gass, I. Harvey, A. D. Newman, K. Wilson and A. F. Lee, *Angew. Chem. Int. Ed.*, 2007, **46**, 8593–8596.
6 B. Qiao, A. Wang, X. Yang, L. F. Allard, Z. Jiang, Y. Cui, J. Liu, J. Li and T. Zhang, *Nat. Chem.*, 2011, **3**, 634–641.
7 M. Yang, L. F. Allard and M. Flytzani-Stephanopoulos, *J. Am. Chem. Soc.*, 2013, **135**, 3768–3771.
8 M. Moses-DeBusk, M. Yoon, L. F. Allard, D. R. Mullins, Z. Wu, X. Yang, G. Veith, G. M. Stocks and C. K. Narula, *J. Am. Chem. Soc.*, 2013, **135**, 12634–12645.
9 P. Hu, Z. Huang, Z. Amghouz, M. Makkee, F. Xu, F. Kapteijn, A. Dikhtiarenko, Y. Chen, X. Gu and X. Tang, *Angew. Chem. Int. Ed.*, 2014, **53**, 3418–3421.
10 A. Bruix, Y. Lykhach, I. Matolínová, A. Neitzel, T. Skála, N. Tsud, M. Vorokhta, V. Stetsovych, K. Ševčíková, J. Mysliveček, R. Fiala, M. Václavů, K. C. Prince, S. Bruyère, V. Potin, F. Illas, V. Matolín, J. Libuda and K. M. Neyman, *Angew. Chem. Int. Ed.*, 2014, **53**, 10525–10530.
11 H. Yan, H. Cheng, H. Yi, Y. Lin, T. Yao, C. Wang, J. Li, S. Wei and J. Lu, *J. Am. Chem. Soc.*, 2015, **137**, 10484–10487.
12 J. Jones, H. Xiong, A. T. DeLaRiva, E. J. Peterson, H. Pham, S. R. Challa, G. Qi, S. Oh, M. H. Wiebenga, X. I. Pereira Hernandez, Y. Wang and A. K. Datye, *Science*, 2016, **353**, 150–154.
13 X. Cui, K. Junge, X. Dai, C. Kreyenschulte, M.-M. Pohl, S. Wohlrab, F. Shi, A. Brückner and M. Beller, *ACS Cent. Sci.*, 2017, **3**, 580–585.
14 Y. Lou and J. Liu, *Ind. Eng. Chem. Res.*, 2017, **56**, 6916–6925.
15 H. Wang, J. Shen, J. Huang, T. Xu, J. Zhu, Y. Zhu and C. Li, *Nanoscale*, 2017, **9**, 16817–16825.
16 M. Piernavieja-Hermida, Z. Lu, A. White, K.-B. Low, T. Wu, J. W. Elam, Z. Wu and Y. Lei, *Nanoscale*, 2016, **8**, 15348–15356.
17 A. M. Gänzler, M. Casapu, P. Vernoux, S. Loridant, F. J. Cadete Santos Aires, T. Epicier, B. Betz, R. Hoyer and J.-D. Grunwaldt, *Angew. Chem. Int. Ed.*, 2017, **56**, 13078–13082.
18 L. Liu, D. N. Zakharov, R. Arenal, P. Concepcion, E. A. Stach and A. Corma, *Nat. Commun.*, 2018, **9**, 574.
19 I. Chorkendorff and J. W. Niemantsverdriet, *Concepts of Modern Catalysis and Kinetics*, Wiley-VCH, Weinheim, 2nd edn., 2007.
20 J. J. H. B. Sattler, J. Ruiz-Martinez, E. Santillan-Jimenez and B. M. Weckhuysen, *Chem. Rev.*, 2014, **114**, 10613–10653.
21 K. Ding, A. Gulec, A. M. Johnson, N. M. Schweitzer, G. D. Stucky, L. D. Marks and P. C. Stair, *Science*, 2015, **350**, 189–192.
22 M. A. Newton, D. Ferri, G. Smolentsev, V. Marchionni and M. Nachtegaal, *Nat. Commun.*, 2015, **6**, 8675.
23 C. Yin, F. R. Negreiros, G. Barcaro, A. Beniya, L. Sementa, E. C. Tyo, S. Bartling, K.-H. Meiwes-Broer, S. Seifert, H. Hirata, N. Isomura, S. Nigam, C. Majumder, Y. Watanabe, A. Fortunelli and S. Vajda, *J. Mater. Chem. A*, 2017, **5**, 4923–4931.
24 P. D. Nellist and S. J. Pennycook, *Science*, 1996, **274**, 413–415.
25 J. H. Kwak, J. Hu, D. Mei, C.-W. Yi, D. H. Kim, C. H. F. Peden, L. F. Allard and J. Szanyi, *Science*, 2009, **325**, 1670–1673.
26 D. Mei, J. H. Kwak, J. Hu, S. J. Cho, J. Szanyi, L. F. Allard and C. H. F. Peden, *J. Phys. Chem. Lett.*, 2010, **1**, 2688–2691.
27 S. A. Bradley, W. Sinkler, D. A. Blom, W. Bigelow, P. M. Voyles and L. F. Allard, *Catal. Lett.*, 2012, **142**, 176–182.
28 W. Sinkler, S. I. Sanchez, S. A. Bradley, J. Wen, B. Mishra, S. D. Kelly and S. R. Bare, *ChemCatChem*, 2015, **7**, 3779–3787.
29 M. Vaarkamp, J. T. Miller, F. S. Modica and D. C. Koningsberger, *J. Catal.*, 1996, **163**, 294–305.
30 J. H. Sinfelt, in *Handbook of heterogenous catalysis*, Eds.: G. Ertl, E.Knözinger, J. Weitkamp, Wiley-VCH, Weinheim, 1997, pp. 1939–1955.
31 F. Pinna, *Catal. Today*, 1998, **41**, 129–137.
32 J.-F. Lambert and M. Che, *J. Mol. Catal. A*, 2000, **162**, 5–18.

33 J. Lynch, *Oil Gas Sci. Technol.*, 2002, **57**, 281–305.
34 J. Regalbuto, *Catalyst Preparation: Science and Engineering*, CRC Press, Boca Raton, 2006.
35 E. Marceau, X. Carrier and M. Che, in *Synthesis of solid catalysts. K.P. De Jong, Ed.*, Wiley-VCH, Weinheim, 2009.
36 P. Munnik, P. E. de Jongh and K. P. de Jong, *Chem. Rev.*, 2015, **115**, 6687–6718.
37 P.-Y. le Goff, W. Kostka and J. Ross, in *Springer Handbook of Petroleum Technology*, Springer, Cham, 2017, pp. 589–616.
38 H. C. Yao, M. Sieg and H. K. Plummer, *J. Catal.*, 1979, **59**, 365–374.
39 D. C. Koningsberger, M. K. Oudenhuijzen, J. H. Bitter and D. E. Ramaker, *Top. Catal.*, 2000, **10**, 167–177.
40 S. I. Sanchez, L. D. Menard, A. Bram, J. H. Kang, M. W. Small, R. G. Nuzzo and A. I. Frenkel, *J. Am. Chem. Soc.*, 2009, **131**, 7040–7054.
41 H. Mistry, F. Behafarid, S. R. Bare and B. Roldan Cuenya, *ChemCatChem*, 2014, **6**, 348–352.
42 A. Gorczyca, V. Moizan, C. Chizallet, O. Proux, W. Del Net, E. Lahera, J.-L. Hazemann, P. Raybaud and Y. Joly, *Angew. Chem. Int. Ed.*, 2014, **53**, 12426–12429.
43 J. Matos, L. K. Ono, F. Behafarid, J. R. Croy, S. Mostafa, A. T. DeLaRiva, A. K. Datye, A. I. Frenkel and B. R. Cuenya, *Phys. Chem. Chem. Phys.*, 2012, **14**, 11457–11467.
44 C. Dessal, PhD thesis, Univ. Lyon, 2018.
45 C. La Fontaine, L. Barthe, A. Rochet and V. Briois, *Catal. Today*, 2013, **205**, 148–158.
46 A. L. Ankudinov, B. Ravel, J. J. Rehr and S. D. Conradson, *Phys. Rev. B*, 1998, **58**, 7565–7576.
47 K. V. Klementev, *J. Phys. D: Appl. Phys.*, 2001, **34**, 209.
48 M. Muñoz, P. Argoul and F. Farges, *Amer. Mineral.*, 2003, **88**, 694–700.
49 G. Kresse and J. Hafner, *Phys. Rev. B*, 1994, **49**, 14251–14269.
50 G. Kresse and J. Furthmüller, *Comput. Mater. Sci.*, 1996, **6**, 15–50.
51 J. P. Perdew, K. Burke and M. Ernzerhof, *Phys. Rev. Lett.*, 1996, **77**, 3865–3868.
52 G. Kresse and D. Joubert, *Phys. Rev. B*, 1999, **59**, 1758–1775.
53 C. H. Hu, C. Chizallet, C. Mager-Maury, M. Corral-Valero, P. Sautet, H. Toulhoat and P. Raybaud, *J. Catal.*, 2010, **274**, 99–110.
54 C. Mager-Maury, C. Chizallet, P. Sautet and P. Raybaud, *ACS Catal.*, 2012, **2**, 1346–1357.
55 M. Digne, P. Sautet, P. Raybaud, P. Euzen and H. Toulhoat, *J .Catal.*, 2002, **211**, 1–5.
56 A. Sangnier, M. Matrat, A. Nicolle, C. Dujardin and C. Chizallet, *J. Phys. Chem. C*, 2018, **122**, 26974–26968.
57 K. Larmier, C. Chizallet, N. Cadran, S. Maury, J. Abboud, A.-F. Lamic-Humblot, E. Marceau and H. Lauron-Pernot, *ACS Catal.*, 2015, **5**, 4423–4437.
58 J. Berdala, E. Freund and J. P. Lynch, *J. Phys. Colloques*, 1986, **47**, C8-269-C8-272.
59 A. Munoz-Paez and D. C. Koningsberger, *J. Phys. Chem.*, 1995, **99**, 4193–4204.
60 F. J. Gracia, J. T. Miller, A. J. Kropf and E. E. Wolf, *J .Catal.*, 2002, **209**, 341–354.
61 Z. Zhang, Y. Zhu, H. Asakura, B. Zhang, J. Zhang, M. Zhou, Y. Han, T. Tanaka, A. Wang, T. Zhang and N. Yan, *Nat. Commun.*, 2017, **8**, 16100.
62 H. Lieske, G. Lietz, H. Spindler and J. Völter, *J. Catal.*, 1983, **81**, 8–16.
63 Y. Xu, W. A. Shelton and W. F. Schneider, *J. Phys. Chem. A*, 2006, **110**, 5839–5846.
64 X. Wang, J. A. van Bokhoven and D. Palagin, *Phys. Chem. Chem. Phys.*, 2017, **19**, 30513–30519.
65 C. Mager-Maury, G. Bonnard, C. Chizallet, P. Sautet and P. Raybaud, *ChemCatChem*, 2011, **3**, 200–207.
66 H. Yoshida, S. Nonoyama, Y. Yazawa and T. Hattori, *Phys. Scr.*, 2005, **2005**, 813.
67 *J .Catal.*, 1993, **144**, 611–626.
68 W. Karim, C. Spreafico, A. Kleibert, J. Gobrecht, J. VandeVondele, Y. Ekinci and J. A. van Bokhoven, *Nature*, 2017, **541**, 68–71.
69 R. M. J. Fiedorow, B. S. Chahar and S. E. Wanke, *Journal of Catalysis*, 1978, **51**, 193–202.
70 S. Duan, R. Wang and J. Liu, *Nanotechnol.*, 2018, **29**, 204002.
71 J. Lin, Y. Chen, Y. Zhou, L. Lin, B. Qiao, A. Wang, J. Liu, X. Wang and T. Zhang, *AIChE J.*, 2017, **63**, 4003–4012.